Front. Phys., 2013, 8(5): 564–576
DOI 10.1007/s11467-013-0373-1

REVIEW ARTICLE

Frontier applications of electrostatic accelerators

Ke-Xin Liu†, **Yu-Gang Wang**, **Tie-Shuan Fan**, **Guo-Hui Zhang**, **Jia-Er Chen**

Institute of Heavy Ion Physics, School of Physics & State Key Laboratory of Nuclear Physics and Technology, Peking University, Beijing 100871, China

Corresponding author. E-mail: †kxliu@pku.edu.cn

Received July 31, 2013; accepted August 8, 2013

Electrostatic accelerator is a powerful tool in many research fields, such as nuclear physics, radiation biology, material science, archaeology and earth sciences. Two electrostatic accelerators, one is the single stage Van de Graaff with terminal voltage of 4.5 MV and another one is the EN tandem with terminal voltage of 6 MV, were installed in 1980s and had been put into operation since the early 1990s at the Institute of Heavy Ion Physics. Many applications have been carried out since then. These two accelerators are described and summaries of the most important applications on neutron physics and technology, radiation biology and material science, as well as accelerator mass spectrometry (AMS) are presented.

Keywords electrostatic accelerator, application, neutron, radiation biology, material science, accelerator mass spectrometry (AMS)

PACS numbers 29.20.Ba, 28.20.Pr, 87.50.-a, 61.80.-x

Contents

1 Introduction 564
2 Electrostatic accelerators 564
2.1 4.5 MV Van de Graaff 564
2.2 EN tandem 565
3 Neutron physics and technology 566
3.1 Cross section and differential cross section measurement for (n, charged-particle) reactions 567
3.2 Excitation function measurement 567
3.3 Development of advanced neutron emission spectrometers 567
4 Radiation related applications 568
4.1 Radiation biology 568
4.2 Applications in material science 570
5 Accelerator mass spectrometry 572
5.1 Xia–Shang–Zhou chronology project 572
5.2 Investigation of Matuyama–Brunhes polarity reversal boundary record 572
5.3 DNA adduction effect with toxic material at environmental low dose levels 573
6 Summary 574
References 574

1 Introduction

Electrostatic accelerator is a powerful tool in many research fields, such as nuclear physics, radiation biology, material science, archaeology and earth sciences. In the Institute of Heavy Ion Physics of Peking University, nuclear technology and application based on accelerator has been developed for more than twenty years as an important research branch. The accelerators providing various ion beams are a 4.5 MV Van de Graaff and an EN tandem with a terminal voltage of 6 MV, while the applications mainly include neutron physics and technology, radiation biology, material science, and accelerator mass spectrometry (AMS). In this paper, we first describe the accelerators and then review the most important applications.

2 Electrostatic accelerators

2.1 4.5 MV Van de Graaff

In order to meet the extensive requirement for various applications of ion beam, it was decided as early as 1976 that a single stage Van de Graaff accelerator should be built at the department of Technical Physics, Peking

© Higher Education Press and Springer-Verlag Berlin Heidelberg 2013

University as a user facility [1]. The design of this machine was completed at Peking University and it was constructed at Xian Feng electro-machinery workshop in Shanghai.

As the largest single stage electrostatic accelerator made in China, the terminal voltage of this machine is 4.5 MV and protons and multiply charged ions can be accelerated with beam currents up to 100 μA. It mainly consists of the high voltage generator, accelerating tube, terminal equipments, control system, isolation gas tank and beam transport system. The high voltage terminal electrode is a kind of smoothly joined spherical and cylindrical surfaces structure with optimized geometrical parameters to ensure the highest field in the surface is less than 1.4 times the ideally optimized field between coaxial cylinders. Charging belt is used to transport charges into terminal with a charging voltage of about 50 kV and the rated charging current is about 400–500 μA. At the early stage, small aperture accelerating tube was adopted. The overall length of the accelerator tube was 3.44 m and it was divided to four sections. Each section consisted of 33 Pyrex glass rings and stainless steel electrodes with two 120° sector openings to keep good gas conductance along the tube. The equipments inside the terminal include ion source, pre-focusing lenses, cross-field analyzer and RF chopper and buncher to produce pulsed beams. The tank is about 8.3 m in height and 2.4 m in diameter and contains a 75% N_2 plus 25% CO_2 mixing isolation gas under a pressure about 12 atms. Ripples and slow drift of the high voltage are detected either by capacitive sensors located near the terminal or by the image slits of the analyzing magnet. The signals are sent to a feedback circuit to control the corana triode and charging voltage source to maintain a stable terminal voltage. Many dipole and quadruple magnets in beam lines transport the ion beams into a neutron target and a radiation target separately.

The installation of the 4.5 MV Van de Graaff was finished in 1988 in the accelerator building at Peking University (Fig. 1). After two years' commissioning, it has been put into operation since 1990 and then a series improvements have been carried out [2–4]. A RF ion source has been installed in the terminal with high proton ratio. The extracted current of hydrogen ions ranges from 240 μA to 500 μA at the exit of ion source and the ratio of $H:H_2$ is more than 80%. A spiral inclined accelerator tube was installed to replace the small aperture tube for higher terminal voltage. The terminal voltage of the machine with new accelerator tube has been reached to 4.6 MV and the stability is better than 0.1%. A beam pulsing system has been developed to meet the need of fast neutron TOF spectroscopy. The beam pulsing system consists of a pair of deflecting plates and a Klystron type buncher inserted between the deflecting plate and the chopping aperture. Pulsed beam with repetition rate of MHz and as short as 2 ns has been obtained. Up to now, the 4.5 Van de Graaff has been operated more than twenty years as a user facility and provides more than 1000 beam hours every year [5].

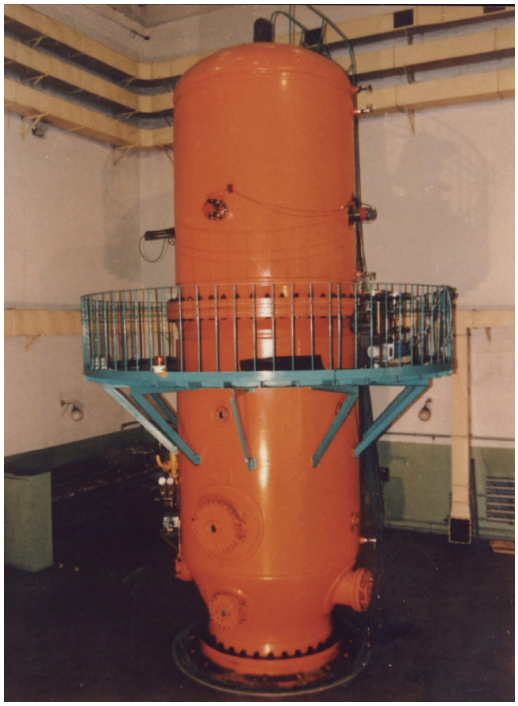

Fig. 1 4.5 MV single stage electrostatic accelerator.

2.2 EN tandem

EN-18 tandem, which has supported many application researches at Peking University, was transferred from Oxford University, UK. As a product of HVEE, it was installed at Oxford University in the early 1960s mainly for the nuclear structure research. In 1980s, nuclear structure research turns to need higher energy and EN tandem became suitable for AMS and radiation researches. Then EN-18 (Fig. 2) came to Beijing in 1986 as a result of the efforts of Prof. Ken Allen and Prof. Jia-Er Chen [6]. After careful dismantling, installation and commissioning, EN tandem was put into operation in 1991 [7, 8]. The whole system consists of negative ion source, injection system, the main accelerator, beam transport lines and ion detector or targets. The terminal voltage has reached to 6 MV and the stability is better than 2 kV. Two beam lines, one is for ion implantation and online analysis and another one is for AMS have been designed and constructed. The heavy ions from ^{10}Be to ^{79}Br can be accelerated to certain energy. The AMS measurement

Fig. 2 EN tandem accelerator.

methods for ^{14}C, ^{10}Be and ^{26}Al have been established since 1993 [9].

Besides providing the beam time more than 1000 hours every year for application researches, the improvements of the machine itself including ion source, injection system, stripper and computer control have been carried out continuously [10–12].

The earliest ion source was a Middelton sputter negative ion source. The main disadvantages of it are the low beam current and few sample targets. For AMS measurements, an ion source with higher beam current and 20 sample targets constructed by the Shanghai Institute of Nuclear Research (SINR) was adopted. Up to 150 μA of carbon beam could be extracted from this ion source, but the sample changing mechanism and electronic control proved unsatisfactory. Consequently, a NEC 40-sample multi-cathode sputter negative ion cesium source (MC SNICS) with a pneumatic sample changing system was installed in 1998 to replace the SINR source. This NEC ion source which has a conical tantalum ionizer and a cesium focus electrode, can provide ion beams with satisfied current and emittance. This ion source is used not only for AMS but also for other experiments.

The original injection system was a dual 30° injection magnet plus a pre-acceleration tube. For AMS measurement, a 90° injection magnet with high resolution was added in front of the dual 30° magnet, the injection beam passed through the 0° port of the dual 30° magnet. Residual magnetic field in the dual 30° magnet occasionally made beam tuning difficult and reduced the beam transmission. In order to simplify the injection system, the position of the AMS 90° injection magnet and the dual 30° magnet has been exchanged. Only two Einzel lenses are required for the new injection beam line. The whole injection system before the pre-acceleration tube is floated on a high voltage of about 50 kV.

Computer control has been developed in order to facilitate accurate adjustment and stable operation. ControlNet (Group 3 Technology Ltd.), which is a fiber-optically linked distributed control system, has been employed. It consists of a loop controller card to handle all the communications on the fiber-optical loop and several device interfaces (DIs). Within each DI there is a processor to handle the loop communications and to service the I/O board. The fiber-optical communication with the DIs provides superior noise immunity, high voltage isolation and fast data transfer. The software has been written with LabView. A main page is used to display all parameters and four subpages are used to control and monitor separate parts of the system. The stabilization of terminal voltage system has been re-designed by using the signal from generation volt meter (GVM) or the image slits of the analyzing magnet. The signals between high voltage and ground are also fiber-optically linked.

The original EN tandem had both gas stripper and foil striper. For reducing emittance expansion, gas stripper was used more frequently. The original gas stripper tube is 700 mm long and 6 mm in diameter. Ar gas was fed into the tube from the middle port and flew out from two ends to the accelerator tube. This made the vacuum worse in the accelerator tube and then reduced the beam transmission efficiency. A recirculation gas stripper has been designed and manufactured for the EN tandem. The gas flowing out from the ends is pumped back to the stripper tube through a middle port. The vacuum in the accelerator tube has been improved remarkably and the diameter of stripper tube is enlarged to 8 mm and the length is shortened to 500 mm. Based on this improvement, the beam transmission of $^{10}Be^{3+}$ has been increased from 5% to 11%, heavy ions with high charge state up to 17 have also been obtained for better fabricating nano structure with ion track technology.

3 Neutron physics and technology

Based on the 4.5 MV Van de Graaff accelerator at Peking University and using solid LiF, Ti-D, Ti-T target and deuterium gas target, mono-energetic neutrons of 20 keV

– 7 MeV and 13–20 MeV can be produced through the ^{7}Li(p,n)^{7}Be, T(p,n)^{3}He, D(d,n)^{3}He and T(d,n)^{4}He reactions which is suitable for high quality nuclear reaction data measurements. The advanced fusion neutron emission spectrometers have been developed and employed for neutron diagnostics at the EAST and HL-2A tokamak devices.

3.1 Cross section and differential cross section measurement for (n, charged-particle) reactions

Cooperated with Frank Laboratory of Neutron Physics, JINR, Dubna, Russia, cross section and differential cross sections for (n, charged-particle) reactions of light, medium mass, and heavy nuclei are measured. Systematic results are obtained.

For light nuclei, measurement of ^{6}Li(n, t)^{4}He and ^{10}B(n, α)^{7}Li reactions are performed in the MeV energy region. "Particle leaking effect" is proved and particle leaking cross sections are determined [13–15]. The results are used for improvement of neutron reaction standards for light elements. For medium mass nuclei, ^{40}Ca, ^{39}K, ^{54}Fe, ^{58}Ni, ^{64}Zn, ^{67}Zn (n, α) reactions and ^{58}Ni, ^{40}Ca(n, p) reactions are measutred (E_n = 3–7 MeV) [16–23]. The neclear data are important both for nuclear engineering and for nuclear reaction model improvement. As for heavy nuclei, cross sections of ^{95}Mo, ^{143}Nd, ^{147}Sm and^{149}Sm (n, α) reactions are quite small and they are measured by using large back-to-back samples [24–27].

For example, ^{149}Sm is one of the most important fission products, with relatively high fission yield. The ^{149}Sm(n, α)^{146}Nd cross section is of interest for nuclear physics, astrophysics as well as nuclear energy applications. However, in the MeV region where the cross section is changing fairly rapidly, there is no measurement datum. Measurements are difficult because activation techniques cannot be used, available neutron fluxes are relatively low, the cross section is fairly small, potential backgrounds can be large, and the sample size is limited by α-straggling considerations. As a result, evaluated nuclear data libraries rely heavily on nuclear model calculations in this region, hence there are very large differences among different library of evaluations. ^{149}Sm (n, α)^{146}Nd cross sections at five energy points in the MeV region are measured. Measurement at 6.0 MeV is repeated with thick and thin samples, and the consistency is achieved after the correction of self-absorption. Small cross section as 50 μb is obtained. Model calculations are also performed, and a good agreement is achieved between measurements and calculations from thermal to MeV energies as shown in Fig. 3 [28].

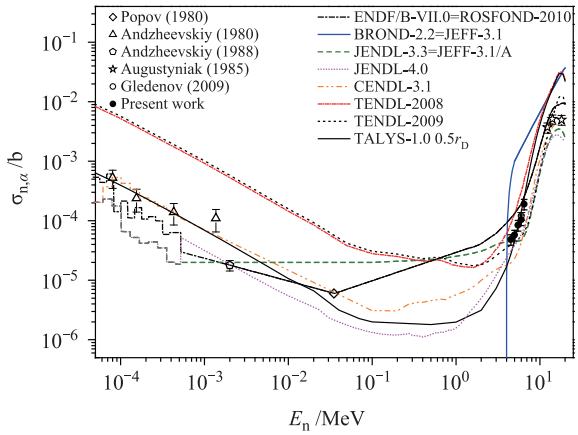

Fig. 3 Measurement of ^{149}Sm (n, α)^{146}Nd cross sections compared with nuclear data library evaluations and TALYS code calculations.

3.2 Excitation function measurement

Neutron activation cross-section data are important for the design and radiation protection of nuclear reactors and ADS systems. Using the activation technique and low background lead chamber, a series of excitation functions of neutron radiative capture, neutron multiplication and charged particle emission reactions are measured, including ^{71}Ga, ^{159}Tb, ^{169}Tm, ^{180}Hf, ^{94}Zr, ^{186}W, ^{75}As, ^{141}Pr (n, γ) reactions (E_n = 0.3–1.6 MeV), ^{58}Ni, ^{60}Ni, ^{64}Zn (n, p) reactions, ^{62}Ni(n, α) reaction, ^{59}Co (n, p), (n, α), (n, 2n) reactions, and ^{88}Y, ^{187}Re, ^{69}Ga(n, 2n) reactions (E_n = 15–20 MeV) [29–34].

For instance, ^{141}Pr is not only an important fission product nuclei, of pertinence in nuclear reactor engineering design, but is also an important rare earth element, used for example in making special type glass and alloy. A number of authors have measured the excitation curve of the cross sections for ^{141}Pr(n, γ)^{142}Pr reaction over the neutron energy of 50 keV to 4.0 MeV, but the discrepancy still exists in the results of different investigators for more than 0.5 MeV neutron energy region. Our measurements are carried out using the activation method. Combined with theoretical calculation, recommend excitation function is given in Fig. 4 [29].

3.3 Development of advanced neutron emission spectrometers

The neutron emission spectrometer (NES) is one of major diagnostic systems in the large tokamak devices such as ITER. Neutron diagnostics of fusion plasmas can be used for the determination of ion temperature, fuel ion composition and fusion power evaluation and even burning plasma diagnostics in future fusion reactor

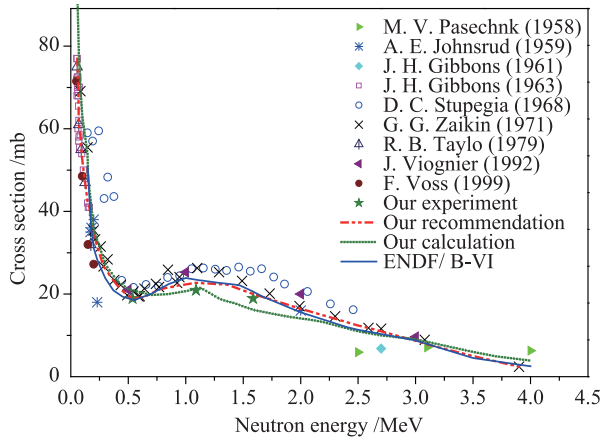

Fig. 4 Comparison of our results of ^{141}Pr(n, γ)^{142}Pr reaction with other measurements and the evaluation data of the ENDF/B-VI in E_n >50 keV.

experiments [35–38].

Organic scintillator spectrometers, based on liquid scintillators and a stilbene crystal detector, the single crystal CVD diamond spectrometer and the neutron camera have been studied and developed on EAST and HL-2A devices for dd fusion neutron diagnostics [39, 40]. New digital pulse shape discrimination techniques, including the digital delay-line-shape (DDLS) method and moment analysis (MA), were presented, and a count rate of about 45 kHz of digital neutron spectrometer has been achieved with good neutron/γ-ray discrimination performances [41, 42]. The important neutron calibrations, such as the light output function measurements of different detectors from the pulse height spectrum, and tests of the proptype spectrometers were carried out by 1.1–17.5 MeV neutrons produced at the 4.5 MeV Van de Graaff accelerator [43, 44].

These advanced neutron emission spectrometers have been employed for the neutron diagnostics of deuterium plasma at HL-2A and EAST [40, 42, 45]. The HL-2A plasma discharges with neutral beam injections were carefully investigated by fusion neutron flux measurements. The plasma ion temperature values on EAST were deduced from the neutron spectra in discharges with lower hybrid wave injection and ion cyclotron resonance heating, and it was the first time to obtain the fuel ion temperature of below 1 keV in takamak devices by NES diagnostics. Figure 5, as an example, shows the neutron energy spectrum measured during shots 41194–41196, and the new world record 32.4 s H-mode plasma has been observed in shot 41195. The ion temperature determined by the NES is about 0.9 keV.

4 Radiation related applications

4.1 Radiation biology

Generally, ionizing radiation (IR) is harmful and potentially lethal to living things. There are two major applications in biology using the accelerators. One is the targeted and non-targeted radiation damage effects in plant. To understand the biological effects of radiation damage induced at different depths of a plant seed, dry or water-imbibed Arabidopsis seeds were irradiated with 1.1 MeV, 2.6 MeV or 6.5 MeV protons (H^+) in comparison with 30 keV nitrogen ions (Fig. 6). The results in Fig. 7 showed that different radiation-induced damages produced at different ranges in Arabidopsis seeds, suggesting there exists a secondary target around the shoot apical meristem (SAM) that also contributes to the radiation response except for the primary target SAM in an Arabidopsis seed [46, 47].

To further investigate the difference between damage caused by non-targeted and direct targeted irradiations, 6.5 MeV protons and 30 keV ^{40}Ar ions were used to irradiate non-shielded or partial-shielded Arabidopsis seeds at different doses. The results showed that excess reactive oxygen species (ROS) are present in the non-irradiated part of the partially irradiated samples, indicating that damage caused by non-targeted effects is different from

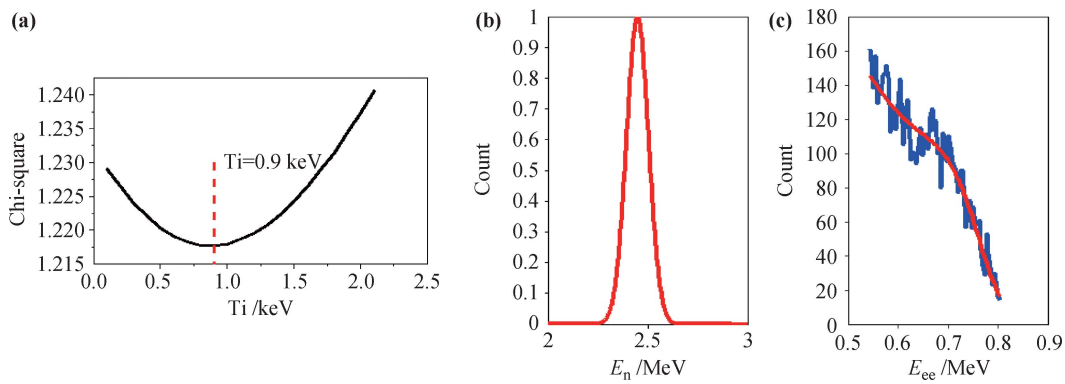

Fig. 5 **(a)** Ion temperature determined from the measurement with NES during shots 41194–41196 on EAST. **(b)** Neutron energy spectra measured with NES. **(c)** Comparison of the measured pulse height spectrum with the reconstructed one.

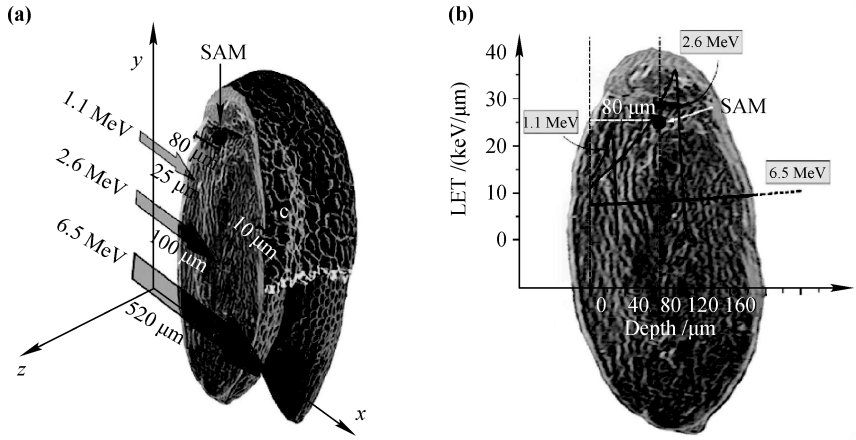

Fig. 6 **(a)** Diagram of an Arabidopsis seed with a cotyledon removed. **(b)** The distribution of LET for each energy of protons versus the position of the SAM.

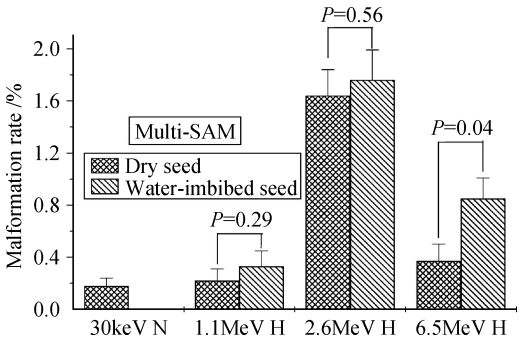

Fig. 7 The multi-SAM malformation rates after irradiation.

that induced by direct irradiation in vivo [48, 49].

The other application of the accelerators in biology, is based on ionizing radiation and has health benefits in radiation therapy for the treatment of cancer. Ionizing radiation has been proven to be a powerful medical treatment in cancer therapy. Rational and effective use of its killing power depends on understanding IR-mediated responses at the molecular, cellular and tissue levels. To understand the DNA double-strand breaks (DSBs) repair efficiency after low and high-LET radiation, synchronous fibroblast normal Human lung fibroblast (NHLF) cells were irradiated with graded doses of proton and γ-ray. The results in Fig. 8 showed that a much slower DSBs repair rate after high LET radiation with protons than that of low-LET radiation with γ-ray, suggesting that the cellular ability to eliminate DSBs after low and high-LET ionizing radiation is quite different [50].

Cancer stem-like cells (CSCs) paradigm suggests that CSCs might have important clinical implications in cancer therapy, for CSCs are suggested to play an important role in tumor radioresistance, recurrence and metastasis. Our and several other studies suggested that there exists an intrinsic homoeostasis state between CSCs and non-CSCs, and radiation can lead to a transient increase of CSC proportion as an initial perturbation on the homoeostasis [51]. To understand the elimination efficiency of CSCs under the radiotherapy used photon, protons as well as carbon irradiation, SW620 colon carcinoma and MCF-7 breast cancer monolayer culture cells were irradiated respectively, the results showed that there was no significantly difference either on long-term clonogenic survival or on short-term apoptosis ratio. However, compared with γ-rays, irradiation with protons was less efficient to accumulate CSCs at the same dose, although both protons and γ-rays can significantly accumulate the CSCs subpopulation, suggesting proton irradiation might have higher efficiency in CSCs elimination for cancer radiotherapy than that of γ-rays (Fig. 9) [52].

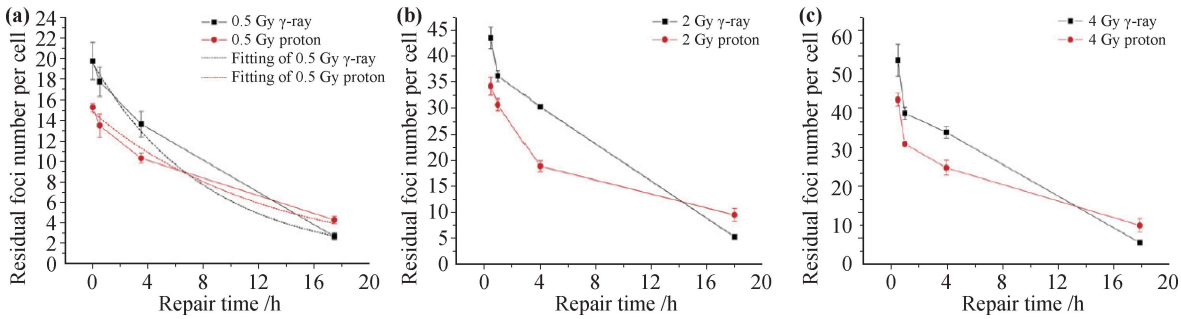

Fig. 8 Scattered diagram and simulation results for foci induction by γ-ray and proton irradiation.

Further studies with sorted CSC and non-CSC from MCF-7 cells showed that CSCs have higher resistance than non-CSCs to either proton or γ-ray irradiation. In addition, compared with γ-ray, proton irradiation is more efficient to kill CSCs at the same dose with lower survival as well as higher DNA damages, suggesting proton irradiation may have greater capability of eliminating CSCs for cancer radiotherapy than γ-ray at the same dose, which in turn may make radiotherapy more efficient [53].

4.2 Applications in material science

Nanoporous membranes are already widely used for filtration and separation in medicine. Etched ion track technique has been developed for decades and is successfully used to fabricate nanoporous polymer membranes. Due to the easy control of the pore diameter and simple fabrication procedure, it is still a promising method. However, inefficiency induced by the thick membrane and inconveniences in integration with "lab-on-a-chip" microfluidics systems impede its development and applications. Recently, we developed a new method to fabricate thin nanoporous silicon dioxide/silicon nitride and silicon nitride membranes using the etched ion track technique. The basic track etching parameters of silicon dioxide and silicon nitride were studied and appropriate irradiation conditions were obtained. The freestanding membranes were obtained by standard silicon fabrication procedures. The multilayer composite silicon/silicon dioxide/silicon nitride was irradiated by Br ions with fluence of 10^8–10^{10} cm^2. The latent ion tracks in silicon dioxide were then etched to the silicon nitride layer by aqueous HF solution (4%) to produce conical nanopores. Subsequently, these nanopores in silicon dioxide layer, acting as a mask, were transferred into the silicon nitride layer by reactive ion etching (RIE). Finally, with an extra HF wet etching step, the nanoporous silicon dioxide/silicon nitride membrane can be thinned to nanoporous silicon nitride membrane, see Fig. 10.

The diameter of the nanopores in silicon nitride can be varied by varying the HF wet etching time. Via this method, nanoporous silicon dioxide/silicon nitride membrane with designed pore density and pore diameter of

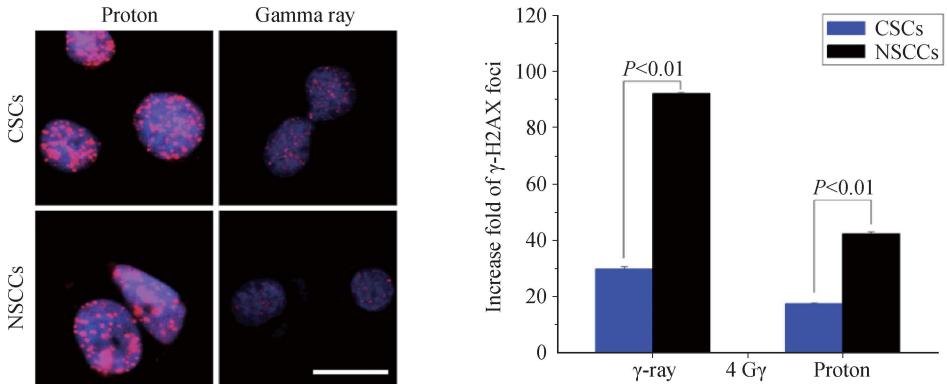

Fig. 9 Representative immunofluorescence and quantification of γ-H2AX foci.

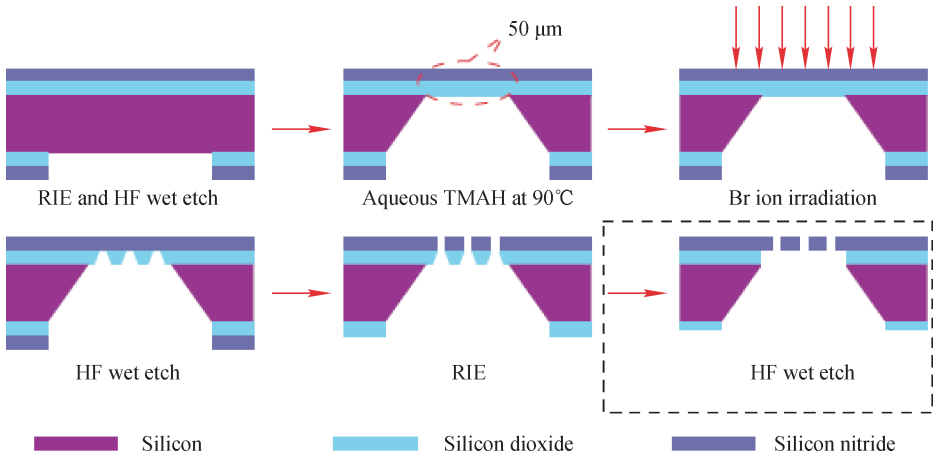

Fig. 10 Schematic fabrication processes of freestanding nanoporous silicon dioxide/silicon nitride membranes.

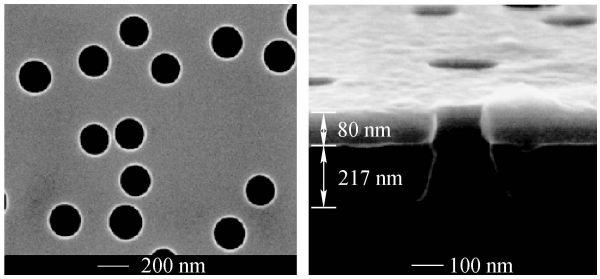

Fig. 11 SEM images of nanoporous silicon dioxide/silicon nitride membranes with ion tracks etched.

sub 100 nm can be achieved (Fig. 11) [54].

The above track-etched silicon nitride nanopores can be shrunk controllably under e-beam irradiation. Our results show that all pores with diameters ranging from 40 to 200 nm can be shrunk, and there is no critical diameter related to the thickness of the membrane (Fig. 12). The shrinkage rate is dependent on the energy deposition rate in the membrane. Based on the e-beam irradiation experiments in the literature and our current results, joule-heat-assisted irradiationinduced diffusion is proposed to be the reason for such shrinkage [55].

Recently, investigation of nuclear materials irradiated by energetic ions becomes an important topic. Materials for fusion reactors will be exposed to severe irradiation environment of heavy atomic displacement damage and a large number of helium and hydrogen atoms. So, it is important to study the synergistic effects of displacement damage and transmutation reaction gas products: helium and hydrogen. Therefore, to simulate the irradiation environment of a fusion reactor, a multi-ion-beam irradiation system was constructed in our institute based on EN tandem and 4.5 MV Von de Graaff accelerator.

With this multi-beam system, 12,18Cr-oxide dispersion strengthened (ODS) steels were irradiated at room temperature by single beam (2.2 MeV He^+ or 3.0 MeV H^+ or 21.0 MeV Si^{4+}), dual-ion-beam (2.2 MeV He^+ and 3.0 MeV H^+) and triple-ion-beam (21.0 MeV Si^{4+}, 2.2 MeV He^+ and 3.0 MeV H^+). Five combination of H, He, He+H, Si, Si+He+H irradiation were used. The mechanical properties of 12,18Cr-ODS steels exhibited that triple-ion-beam irradiation could strengthen irradiation swelling and hardening effect. Carbon segregation and several new carbon peaks appeared in the Raman spectrum of irradiated 12Cr-ODS steel. A clear correlation was established between the carbon distribution and the damage distribution [56].

In addition, single crystal 6H–SiC irradiated by Si^{3+}/He^+ coimplantation was studied to analyze changes in structural and optical properties by Raman spectroscopy shown in Fig. 13, UV–visible transmittance spectroscopy and Fourier transform infrared reflectance. Four ion irradiation experiments were performed, He^+ (single), Si^{3+} (single), Si^{3+} + He^+ (successively) and

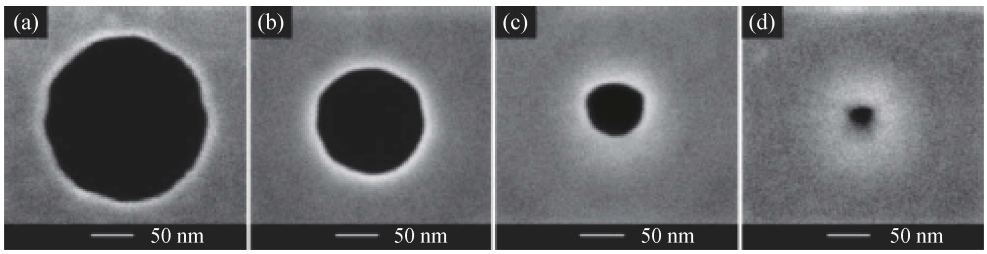

Fig. 12 In situ imaging of a 190 nm silicon nitride nanopore using the SEM electron beam accelerated at 15 kV.

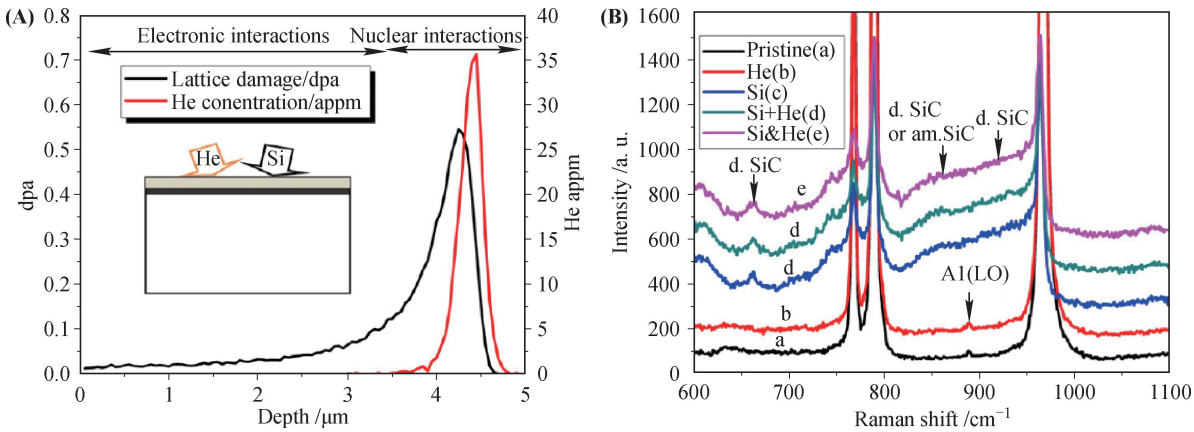

Fig. 13 **(A)** SRIM 2008 simulation of lattice damage in SiC implanted with 18 MeV Si^{3+} and depth distribution of 2.2 MeV He^+ concentration and **(B)** Raman scattering spectra of Si^{3+}/ He^+ coimplantation SiC at RT.

Si^{3+} & He^{+} (simultaneously). The fluences for 18 MeV Si^{3+} and 2.2 MeV He^{+} at the damage peak are 0.55 dpa and 35 appm, respectively. The synergistic effect due to Si^{3+} and He^{+} simultaneously implanted into SiC is higher than that of sequential irradiation. Helium will aggravate irradiation damage when it is introduced into SiC. Defects such as vacancies due to displacement damage stabilized by helium are related to the optical absorption band. Optical defects induced by heavy ions are related to elastic collisions which occur at the nuclear energy loss region. Simultaneous recovery of defects due to dynamic annealing effects resulting from the excessive heat induced by dual-ion irradiation was observed [57].

5 Accelerator mass spectrometry

Accelerator mass spectrometry (AMS) is a powerful means to measure the isotopic abundance of long-lived radionuclides. Apart from their use in dating, the cosmogenic nuclides can also be used as a powerful tracer to track changes in the terrestrial or marine environmental systems. Since AMS measurement methods for ^{14}C, ^{10}Be and ^{26}Al was established in 1993 based on EN tandem, thousands of samples have been measured and many application projects have been carried out in the fields of archaeology, earth sciences, environmental science and biomedical sciences. Here we only introduce several typical and important examples.

5.1 Xia–Shang–Zhou chronology project

Chinese ancient civilization has been lasting for several thousand years without interruption. It is well known that the earliest dynasties of China are Xia, Shang and Zhou. However, there have been many arguments on the particular dates of Xia and Shang dynasties because there was no complete chronology in well recognized literatures before 841BC. A radiocarbon dating campaign was performed by archaeologists and radiocarbon dating experts in China from 1996 and the objective was to establish a chronological framework for Xia, Shang and Zhou based on scientific evidences [58].

The radiocarbon ages obtained by dedicated AMS can be very precise with uncertainty as small as less than 30 years. However, the calibration of radiocarbon age to calendar age with the tree ring calibration curve will enlarge the error in most cases due to the wiggles on the calibration curve, and the specific error of calendar age depends on the curve shape. Therefore, the radiocarbon dating of individual sample may not always meet the requirement for an accurate and precise chronology. However for a series of samples with certain sequence, Bayesian method can be used for calibration and the errors of the calendar age can be substantially reduced. Using this method, the archaeological samples unearthed from a site are grouped into different phases according to their cultural characteristics and sufficient samples are needed for each phase.

More than 200 samples in series collected from 7 archaeological sites such as Fengxi [59] and Xinzhai [60] were dated by AMS at Peking University and the results were calibrated with OxCal. Figure 15 shows the calibration curve of Xinzhan site. A chronological framework of Xia, Shang and Zhou Dynasties was then established on the basis of the radiocarbon dating results and the astronomical analysis, which showed that the Xia Dynasty lasted from about 2070–1600 cal BC, the Shang Dynasty was from 1600–1046 cal BC and the Zhou Dynasty was from 1046–771 cal BC.

In the project of Xia–Shang–Zhou Chronology, most interesting work is dating the oracle bones. Oracle bones were discovered about 100 years ago and most of them were excavated around Yin site in Henan Province, China. Most of the oracle bones were made of ox shoulder blade and some tortoise shell. There are inscriptions on many oracle bones which recorded the auspicial prediction and subsequent events in ancient Chinese history. The names of the nine Kings of late Shang Dynasty, from King Wuding to King Dixin, can be found in the oracle inscriptions. Many oracle bone samples were dated by AMS at Peking University. Only a small piece of about 1 square centimeter was cut from the part without inscriptions of each oracle bone (Fig. 14). The obtained AMS ^{14}C ages provided key data for establishing an accurate chronology for late Shang Dynasty in early Chinese history [58].

5.2 Investigation of Matuyama–Brunhes polarity reversal boundary record

^{10}Be produced in the atmosphere is soon attached to mineral aerosols and deposited on the earth surface by precipitation. It is a useful isotopic tracer for investigating the formation of Aeolian deposits and Quaternary climate evolution. The Matuyama–Brunhes polarity reversal which happened 0.78 Ma ago was recorded in loess L8 in Chinese loess sequence. This corresponds to a glacial period and is obviously different from the marine record where the same reversal boundary has been found in the sediments of Oxygen Isotope Stage 19, an interglacial period. One explanation is that the loess record of the Matuyama–Brunhes boundary (MBB) is displaced downwards by over 100 cm [61]. In order to determine the true position of the MBB in loess, ^{10}Be concentration in

Fig. 14 Oracle bones dated by AMS.

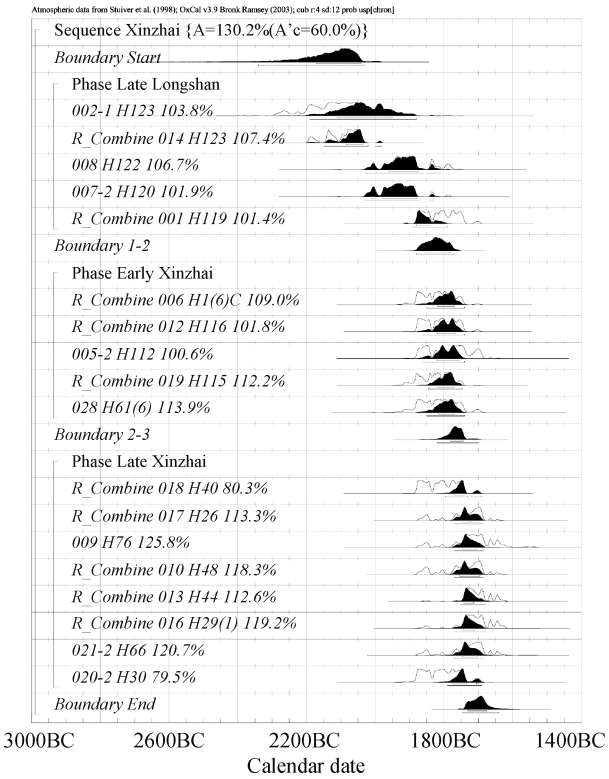

Fig. 15 Oxcal calibration plot of Xinzhai site samples.

loess from Louchuan, Shanxi Province has been investigated by AMS ^{10}Be measurements at Peking University based on the assumption that the increase of the ^{10}Be production rate due to the reduction of geomagnetic field intensity during the polarity reversal is significant and can be recorded in the loess sequence. More than 200 ^{10}Be samples from Louchuan loess has been measured and the preliminary result shows an obvious displacement of the loess record of the Matuyama–Brunhes boundary.

5.3 DNA adduction effect with toxic material at environmental low dose levels

AMS is a powerful tool to study the adduction effect between the toxic materials at environmental low dose levels and bio-macromolecules such as DNA and Hemoglobin (Hb). Nicotine is a major alkaloid in tobacco products and has proven to be a potential geno-toxic compound. DNA adduction with ^{14}C-labeled nicotine and nicotine-derived nitrosamine NNK was investigated in mouse liver at doses equivalent to low-level exposure of humans [62]. In the exposure of mice to either nicotine or NNK, the number of DNA adducts increased linearly with increasing dose. This result showed that nicotine is a potential carcinogen. But many natural dietary products can suppress the DNA adduction, and hence act as inhibitors of cancer. The inhibitory effects of curcumin, garlic squeeze, grape-seed extract, tea polyphenols, vitamin C and vitamin E on nicotine-DNA adduction have been investigated using AMS [63]. The results demonstrated that all these dietary constituents induced marked dose-dependent decrease in nicotine-DNA

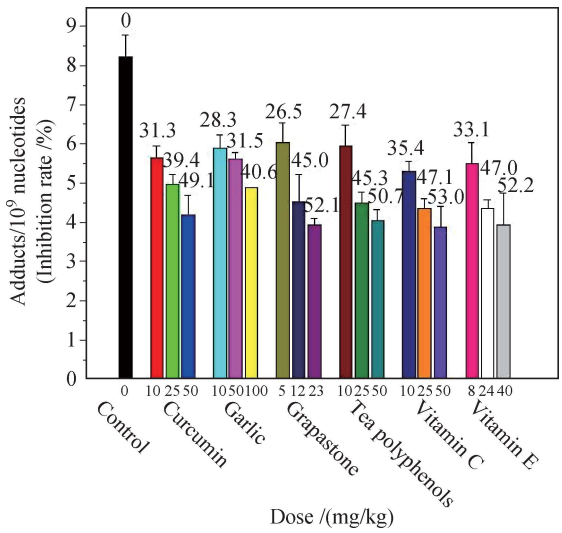

Fig. 16 The inhibitory effects of curcumin, garlic squeeze, grape-seed extract, tea polyphenols, vitamin C and vitamin E on nicotine-DNA adduction.

adducts as compared with the control (Fig. 16). The reduction rate reached about 50% for all agents, except garlic squeeze (40%), even at its highest dose level. Amongst the six agents, grape-seed extract exhibited the strongest inhibition to the DNA adduct formation.

This kind of research was extended to nitrobenzene, Methyl tart-butyl ether (MTBE) and acryl amide (AA). For example, potential molecular toxicity of acrylamide (AA) was evaluated [64]. The lowest doses taken by mice are 7.5 × 10-2 and 7.5 × 10-1 μg/kg b.w., which are very close to the WHO published data of the average daily intake of AA for the general population. The results of AA-protamine, AA-sperm DNA and AA-sperm head/tail adducts at low dose levels suggest that the quality of sperm might be damaged gradually by adducts of AA in the sperm compositions followed by cumulate daily AA exposure.

6 Summary

4.5 MV Van de Graaff and EN tandem at the Institute of Heavy Ion Physics have been operated stably for more than 20 years and fruitful application achievements based on these two electrostatic accelerators have been obtained. With the technique development such as accurate beam scanning and multi-beam to one target, more attractive application works are expected.

References

1. J. E. Chen and Y. X. Zhang, Design of 4.5 MV electrostatic accelerator, Proceeding of the first Japan–China Joint Symposium on Particle Accelerators and their Applications in Nuclear Research and Industry, University of Tokyo, Japan, 1980: 19
2. J. E. Chen, Y. X. Zhang, J. Y. Wang, et al., Progress and application of the 4.5 MV electrostatic accelerator, Proceeding of the fifth Japan–China Joint Symposium on Particle Accelerators and their Applications in Nuclear Research and Industry, University of Osaka, Japan, 1993: 174
3. L. H. Gong, et al., The 4.5 MV single stage electrostatic accelerator, *Modern Scientific Instruments*, 1995 (2): 9
4. J. Q. Lu and S. W. Quan, Beam pulsing system for the 4.5 MV electrostatic accelerator, *Nucl. Instrum. Methods A*, 1995, 346: 31
5. J. Y. Wang, L. H. Gong, X. J. Yang, et al., Operation and improvement of the 4.5 MV electrostatic accelerator at Peking University, *Atomic Science and Technology*, 2008, 42(Suppl.): 239
6. A. E. Litherland and K. Allen, Oxford, Beijing and AMS, *Nucl. Instrum. Methods B*, 2000, 172(1–4): 721
7. J. E. Chen, Z. Y. Guo, S. Q. Yan, et al., Status of the tandem accelerator mass spectrometry at Peking University, *Nucl. Instrum. Methods B*, 1990, 52: 306
8. J. X. Yu, R. X. Li, L. H. Gong, et al., The operation and improvements of the EN tandem at Peking University, *Nucl. Technol.*, 1992, 15(6): 335
9. J. E. Chen, Z. Y. Guo, S. Q. Yan, R. Li, M. Xiao, K. Li, H. Liu, K. Liu, J. Wang, B. Li, X. Lu, S. Yuan, T. Chen, S. Gao, S. Zheng, C. Chen, and Y. Liu, Accelerator mass spectrometry at Peking University: Experiments and progress, *Nucl. Instrum. Methods B*, 1994, 92(1–4): 47
10. L. H. Gong, Y. X. Shen, X. J. Yang, et al., The control and monitor system of EN tandem at Peking University, *Nucl. Technol.*, 1993, 16(9): 561
11. K. X. Liu, Z. Y. Guo, X. Y. Lu, et al., Improvements of PKUAMS for precition ^{14}C analysis of the project of Xia–Shang–Zhou chronology, *Nucl. Instrum. Methods B*, 2000, 172: 70
12. K. X. Liu, Z. Zhu, L. H. Gong, et al., A new recirculation gas stripper for EN tandem, *Nucl. Technol.*, 2007, 30(12): 1
13. G. Zhang, J. Chen, G. Tang, et al., Measurement of differential and angle-integrated cross sections of the ^{6}Li(n,t)^{4}He reaction in the MeV neutron energy range, *Nucl. Instrum. Methods A*, 2006, 566(2): 615
14. G. Zhang, L. Guo, R. Cao, J. Zhang, and J. Chen, Cross-section measurement for the ^{10}B(n, α)^{7}Li reaction at 4.0 and 5.0 MeV, *Appl. Radiat. Isot.*, 2008, 66(10): 1427
15. G. H. Zhang, X. Liu, J. M. Liu, Z. H. Xue, H. Wu, and J. X. Chen, Measurement of cross sections for the ^{10}B(n, α)^{7}Li reaction at 4.0 and 5.0 MeV using asymmetrical twin gridded ionization chamber, *Chin. Phys. Lett.*, 2011, 28(8): 082801
16. X. Zhang, Z. Chen, Y. Chen, J. Yuan, G. Tang, G. Zhang, J. Chen, Y. Gledenov, G. Khuukhenkhuu, and M. Sedysheva, Dispersion relations for (n,n), (n,p), and (n, α) reactions on ^{39}K and ^{40}Ca, *Phys. Rev. C*, 2000, 61(5): 054607
17. G. Zhang, J. Zhang, R. Cao, et al., Measurement of differential cross section for the ^{64}Zn(n, α)^{61}Ni reaction at 2.54, 4.00 and 5.50 MeV, *Nucl. Sci. Eng.*, 2008, 160(1): 123
18. G. Zhang, R. Cao, J. Chen, et al., Differential cross-section measurement for the ^{64}Zn(n, α)^{61}Ni reaction at 5.03 and 5.95 MeV, *Nucl. Sci. Eng.*, 2007, 156(1): 115
19. G. Tang, G. H. Zhang, J. X. Chen, et al., Tests of the GIC and Measurement of Angular Distribution and Energy Spectra for ^{58}Ni(n, p)^{58}Co at 4.1 MeV, INDC(CPR)-043/L, 1997, 18: 1
20. G. Y. Tang, J. H. Fan, J. X. Chen, et al. Measurement of Angular Distribution at 6.0–7.0 MeV for ^{58}Ni(n, α)^{55}Fe and ^{54}Fe(n, α)^{51}Cr, INDC(CPR)-042/L, 1997, 17: 1
21. G. Y. Tang, D. C. Qu, W. G. Zhong, et al., Cross section measurements for ^{40}Ca(n, α)^{37}Ar reaction, *Chinese J. Nucl. Phys.*, 1993, 15(3): 239
22. G. H. Zhang, H. Wu, J. G. Zhang, J. M. Liu, J. X. Chen, Yu. M. Gledenov, M. V. Sedysheva, G. Khuukhenkhuu, and P. J.

Szalanski, Cross-section measurement for the ^{67}Zn(n, α)^{64}Ni reaction at 6.0MeV, *Eur. Phys. J. A*, 2010, 43(1): 1

23. G. H. Zhang, Yu. M. Gledenov, G. Khuukhenkhuu, M. V. Sedysheva, P. J. Szalanski, J. Liu, H. Wu, X. Liu, J. Chen, and V. A. Stolupin, Cross sections of the ^{67}Zn(n, α)^{64}Ni reaction at 4.0, 5.0, and 6.0 MeV, *Phys. Rev. C*, 2010, 82(5): 054619
24. G. Zhang, J. Zhang, L. Guo, H. Wu, J. Chen, G. Tang, Y. M. Gledenov, M. V. Sedysheva, G. Khuukhenkhuu, and P. J. Szalanski, Measurement of cross sections for the ^{147}Sm(n, α)^{144}Nd reaction at 5.0 and 6.0 MeV, *Appl. Radiat. Isot.*, 2009, 67(1): 46
25. Yu. M. Gledenov, M. V. Sedysheva, V. A. Stolupin, G. H. Zhang, J. G. Zhang, H. Wu, J. Liu, J. Chen, G. Khuukhenkhuu, P. E. Koehler, and P. J. Szalanski, Cross sections of the ^{143}Nd(n, α)^{140}Ce and ^{147}Sm(n, α)^{144}Nd reactions in the MeV neutron energy region, *Phys. Rev. C*, 2009, 80(4): 044602
26. G. H. Zhang, H. Wu, J. G. Zhang, J. M. Liu, Y. X. Yin, J. X. Chen, Y. M. Gledenov, M. V. Sedysheva, G. Khuukhenkhuu, P. E. Koehler, and P. J. Szalanski, Cross section measurement for the ^{95}Mo(n, α)^{92}Zr reaction at 4.0, 5.0 and 6.0 MeV, *Appl. Radiat. Isot.*, 2010, 68(1): 180
27. Yu. M. Gledenov, G. H. Zhang, G. Khuukhenkhuu, M. V. Sedysheva, P. J. Szalanski, P. E. Koehler, J. M. Liu, H. Wu, X. Liu, and J. X. Chen, Cross-section measurement and analysis for the ^{149}Sm(n, α)^{146}Nd reaction at 6.0 MeV, *Phys. Rev. C*, 2010, 82(1): 014601
28. G. H. Zhang, Y. M. Gledenov, G. Khuukhenkhuu, M. V. Sedysheva, P. J. Szalanski, P. E. Koehler, Y. N. Voronov, J. M. Liu, X. Liu, J. Han, and J. Chen, ^{149}Sm(n, α)^{146}Nd cross sections in the MeV region, *Phys. Rev. Lett.*, 2011, 107(25): 252502
29. P. Zhu, Z. Yuan, J. Chen, Z. Liu, G. Zhang, Z. Shi, and H. Lu, Measurement of neutron capture cross sections for ^{141}Pr from 0.5 to 1.6 MeV, *Appl. Radiat. Isot.*, 2007, 65(12): 1314
30. J. X. Chen, Z. M. Shi, G. Y. Tang, et al., Measurement of ^{64}Zn(n, γ)^{65}Zn cross sections, *Chinese J. Nucl. Phys.s*, 1995, 17(4): 342 (J)
31. J. X. Chen, Z. M. Shi, G. Y. Tang, et al., Measurement of neutron capture cross section for ^{180}Hf, *Chinese J. Nucl. Phys.*, 1997, 19(2): 110
32. J. X. Chen, Z. M. Shi, G. Y. Tang, et al., Measurement of fast-neutron capture cross sections for ^{159}Tb and ^{169}Tm, *Nucl. Sci. Tech.*, 1998, 9(3): 138
33. G. H. Zhang, Z. M. Shi, G. Y. Tang, et al., Interference of the low-energy neutrons on activation cross section measurement of the ^{186}W(n, γ)^{187}W reaction, *Nucl. Sci. Eng.*, 2001, 137(1): 107 (J)
34. G. H. Zhang, Z. M. Shi, G. Y. Tang, et al., Measurement of fast-neutron capture cross sections for ^{75}As, *Nucl. Sci. Tech.*, 2001, 12(3): 161
35. Q. L. Ni, X.G. Wang, C. Zhang, and T. S. Fan, A full-f calculation of spontaneous toroidal rotation in H-mode plasma, *Plasma Phys. Contr. Fusion*, 2012, 53(8)
36. Q. L. Ni, T. S. Fan, X. Zhang, C. Zhang, Q. L. Ren, and C. D. Hu, Predictive calculation of neutral beam heating plasmas in EAST tokamak by NUBEAM code for certain parameter ranges, *Plasma Science Tech.*, 2010, 12(6): 661
37. Z. J. Chen, T. S. Fan, C. Zhang, C. D. Hu, and X. G. Wang, Simulation of EAST off-axis neutral beam heating and current drive, *Fusion Eng. Design*, 2012, 87: 325
38. Z. Chen, M. Nocente, M. Tardocchi, T. Fan, and G. Gorini, Simulation of neutron emission spectra from neutral beamheated plasmas in the EAST tokamak, *Nucl. Fusion*, 2013, 53(6): 063023
39. X. F. Xie, X. Zhang, X. Yuan, T. S. Fan, J. X. Chen, and X. Q. Li, Investigation of the influence of a ninner gas bubble on the response of a liquid scintillation detectorto g-rays and neutrons, *Nucl. Instrum. Methods A*, 2013, 721: 10
40. X. Zhang, X. Yuan, X. F. Xie, Z. J. Chen, X. Y. Peng, J. X. Chen, G. H. Zhang, X. Q. Li, T. S. Fan, G. Q. Zhong, L. Q. Hu, and B. N. Wan, A compact stilbene crystal neutron spectrometer for EAST D-D plasma neutron diagnostics, *Rev. Sci. Instrum.*, 2013, 84(3): 033506
41. X. F. Xie, X. Zhang, X. Yuan, J. X. Chen, X. Q. Li, G. H. Zhang, T. S. Fan, G. L. Yuan, J. W. Yang, and Q. W. Yang, Digital discrimination of neutrons and gamma-rays in organic scintillation detectors using moment analysis, *Rev. Sci. Instrum.*, 2012, 83(9): 093507
42. X. Zhang, X. Yuan, X. F. Xie, Z. J. Chen, J. X. Chen, T. S. Fan, G. L. Yuan, J. W. Yang, and Q. Q. Yang, A digital delay-line-shaping methods for pulse shape discrimination in stilbene neutron detector and application to fusion neutron measurement at HL-2A tokamak, *Nucl. Instrum. Methods A*, 2012, 687: 7
43. X. Zhang, X. Yuan, X. Xie, T. Fan, J. Chen, and X. Li, The design and optimization of a neutron time-of-flight spectrometer with double scintillators for neutron diagnostics on EAST, *Plasma Science Tech.*, 2012, 14(7): 675
44. X. Xie, X. Yuan, X. Zhang, T. Fan, J. Chen, and X. Li, Calibration and unfolding of the pulse height spectra of liquid scintillator-based neutron detectors using photon sources, *Plasma Science Tech.*, 2012, 14(6): 553
45. X. Yuan, X. Zhang, X. Xie, G. Gorini, Z. Chen, X. Peng, J. Chen, G. Zhang, T. Fan, G. Zhong, L. Hu, and B. N. Wan, Neutron energy spectrum measurements with a compact liquid scintillation detector on EAST, *J. Instrumentation*, 2013, 8: P07016
46. H. Qin, J. Xue, F. He, J. Lai, W. Zhang, J. Wang, S. Yan, W. Zhao, H. Gu, and Y. Wang, Biological effect of the seeds of Arabidopsis thaliana irradiated by MeV protons, *Radiation Effects and Defects in Solids: Incorporating Plasma Science and Plasma Technology*, 2006, 160(3–4): 131
47. H. L. Qin, Y. G. Wang, J. M. Xue, Q. Miao, L. Ma, T. Mei, W. M. Zhang, W. Guo, J. Y. Wang, and H. Y. Gu, Biological effects of protons targeted to different ranges in Arabidopsis seeds, *Int. J. Radiat. Biol.*, 2007, 83(5): 301

48. G. Yang, T. Mei, H. Yuan, W. Zhang, L. Chen, J. Xue, L. Wu, and Y. Wang, Bystander/abscopal effects induced in intact Arabidopsis seeds by low-energy heavy-ion radiation, *Radiat. Res.*, 2008, 170(3): 372
49. T. Mei, G. Yang, Y. Quan, W. Wang, W. Zhang, J. Xue, L. Wu, H. Gu, G. Schettino, and Y. Wang, Oxidative metabolism involved in non-targeted effects induced by proton radiation in intact Arabidopsis seeds, *J. Radiat. Res.*, 2011, 52(2): 159
50. J. Wu, Q. Fu, Y. Quan, W. Wang, T. Mei, J. Li, G. Yang, X. Ren, J. Xue, and Y. Wang, Repair rates of DNA double-strand breaks under different doses of proton and g-ray irradiation, *Nucl. Instrum. Methods B*, 2012, 276: 1
51. G. Yang, Y. Quan, W. Wang, Q. Fu, J. Wu, T. Mei, J. Li, Y. Tang, C. Luo, Q. Ouyang, S. Chen, L. Wu, T. K. Hei, and Y. Wang, Dynamic equilibrium between cancer stem cells and non-stem cancer cells in human SW620 and MCF-7 cancer cell populations, *Br. J. Cancer*, 2012, 106(9): 1512
52. Q. Fu, Y. Quan, W. Wang, T. Mei, J. Wu, J. Li, G. Yang, X. Ren, J. Xue, and Y. Wang, Response of cancer stem-like cells and non-stem cancer cells to proton and g-ray irradiation, *Nucl. Instrum. Methods B*, 2012, 286: 346
53. Y. Quan, W. Wang, Q. Fu, T. Mei, J. Wu, J. Li, G. Yang, and Y. Wang, Accumulation efficiency of cancer stem-like cells post g-ray and proton irradiation, *Nucl. Instrum. Methods B*, 2012, 286: 341
54. W. Zhang, J. Li, L. Cao, Y. Wang, W. Guo, K. Liu, and J. Xue, Fabrication of nanoporous silicon dioxide/silicon nitride membranes using etched ion track technique, *Nucl. Instrum. Methods B*, 2008, 266(12–13): 3166
55. W. Zhang, Y. Wang, J. Li, M. Xu, H. Ji, Q. Ouyang, J. Xu, and Y. Zhang, Controllable shrinking and shaping of silicon nitride nanopores under electron irradiation, *Appl. Phys. Lett.*, 2007, 90(16): 163102
56. Y. Zhang, X. Qian, X. Wang, S. Liu, C. Wang, T. Li, Z. Zhao, and D. Lu, Mechanical and Raman spectroscopic studies of multi-ion-beam irradiated 12,18Cr-oxide dispersion strengthened steels, *Nucl. Instrum. Methods B*, 2013, 297: 35
57. X. Wang, Y. Zhang, S. Liu, C. Wang, and Z. Zhao, Optical and structural properties of 6H–SiC irradiated by Si3t n Het coimplantation, *Nucl. Instrum. Methods B*, 2012, 289: 47
58. Z. Guo, K. Liu, X. Lu, et al., The use of AMS radiocarbon dating for Xia–Shang–Zhou chronology, *Nucl. Instr. Meth. B*, 2004, 223–224: 168
59. Z. Guo, K. Liu, S. Yuan, et al., AMS radiocarbon dating of Fengxi site in Shaanxi, China, *Radiocarbon*, 2005, 47(2): 221
60. K. Liu, B. Han, Z. Guo, et al., AMS Radiocarbon dating of bone samples from Xinzhai site in China, *Radiocarbon*, 2005, 47(1): 221
61. K. X. Liu, H. L. Gao, L. P. Zhou, F. Xu, S. X. Peng, J. L. Yuan, and Z. Y. Guo, AMS mearsurements of 10Be concentration in Chinese loess using PKUAMS, *Nucl. Instr. Meth. B*, 2004, 223–224: 168
62. X. S. Li, F. Wang, J. Y. Shi, et al., Genotoxicity study on nicotine and nicotine-derived nrator mass spectrometry, *Radiocarbon*, 1996, 38(2): 347
63. Y. Cheng, H. L. Li, H. F. Wang, H. F. Sun, Y. F. Liu, S. X. Peng, K. X. Liu, and Z. Y. Guo, Inhibition of nicotine-DNA adduct formation in mice by six dietary constituents, *Food Chem. Toxicol.*, 2003, 41(7): 1045
64. Q. Xie, Y. Liu, H. F. Sun, et al., Inhibition of acrylamide toxicity in mice by three dietary constituents, *Toxicol. Lett.*, 2006, 163: 101